A&A manuscript no.
(will be inserted by hand later)

Your thesaurus codes are:
02(02.19.1;02.08.1;02.18.7)

ASTRONOMY AND ASTROPHYSICS
September 27, 2000

The structure of radiative shock waves

III. The partially ionized hydrogen gas

Yu.A. Fadeyev[1] **and D. Gillet**[2]

[1] Institute for Astronomy of the Russian Academy of Sciences, Pyatnitskaya 48, 109017 Moscow, Russia
email: fadeyev@inasan.rssi.ru

[2] Observatoire de Haute-Provence - CNRS, F-04870 Saint-Michel l'Observatoire, France
email: gillet@obs-hp.fr

Received September 2000 / Accepted

Abstract. The grid of the models of radiative shock waves propagating through the partially ionized hydrogen gas with temperature 3000K $\le T_1 \le$ 8000K and density 10^{-12} gm cm^{-3} $\le \rho_1 \le 10^{-9}$ gm cm^{-3} is computed for shock velocities 20 km s^{-1} $\le U_1 \le$ 90 km s^{-1}. The fraction of the total energy of the shock wave irreversibly lost due to radiation flux ranges from 0.3 to 0.8 for 20 km s^{-1} $\le U_1 \le$ 70 km s^{-1}. The postshock gas is compressed mostly due to the radiative cooling in the hydrogen recombination zone and final compression ratios are within $1 < \rho_N/\rho_1 \lesssim 10^2$ depending mostly on the shock velocity U_1. The preshock gas temperature affects the shock wave structure due to the equilibrium ionization of the unperturbed hydrogen gas since the rates of postshock relaxation processes are very sensitive to the number density of hydrogen ions ahead the discontinuous jump. Both the increase of the preshock gas temperature and the decrease of the preshock gas density lead to lower postshock compression ratios. The width of the shock wave decreases with increasing upstream velocity while the postshock gas is still partially ionized and increases as soon as the hydrogen is fully ionized. All shock wave models exhibit the stronger upstream radiation flux emerging from the preshock outer boundary in comparison with downstream radiation flux emerging in opposite direction from the postshock outer boundary. The difference between these fluxes depends on the shock velocity and ranges from 1% to 16% for 20 km s^{-1} $\le U_1 \le$ 60 km s^{-1}. The monochromatic radiation flux transported in hydrogen lines significantly exceeds the flux of the background continuum and all shock wave models demonstrate the hydrogen lines in emission.

Key words: Shock waves – Hydrodynamics – Radiative transfer – Stellar atmospheres

1. Introduction

Main indicators of shock waves in atmospheres of radially pulsating stars are the enhanced hydrogen emission, double profiles of absorption lines and discontinuities in radial velocity curves. Most prominently these features are observed in W Vir (Lèbre & Gillet, 1992), RV Tau (Gillet et al., 1989) and Mira type (Alvarez et al., 2000) pulsating variables. The ratio of the atmosphere scale height to the stellar radius in these stars is $H/R \gtrsim 10^{-2}$ and the linear theory of stellar pulsation admits the existence of progressive waves propagating through the stellar atmosphere (Unno, 1965; Pijpers, 1993). The running waves must inevitably transform into shock waves due to nonlinear effects and this conclusion is corroborated by hydrodynamic calculations of radial pulsations of low–mass late–type giants (Wood, 1974; Fadeyev & Tutukov, 1981; Bowen, 1988; Fadeyev & Muthsam, 1990).

Periodic shock waves drive gas outflows in atmospheres of late–type giants that lead to the mass loss and very often to the formation of circumstellar dust shells. It must be noted that the postshock velocity near the photosphere should not be necessarily greater than the local escape velocity because periodic passage of shock waves distends the stellar atmosphere and, under some conditions, may lead to the gradual approach of the gas flow to the escape velocity (Willson & Hill, 1979). Furthermore, the shock amplitude tends to enhance while the shock wave propagates in the medium with decaying gas density.

The most outstanding problem concerning the shock–driven mass loss is the rate of the shock decay during its passage through the stellar atmosphere. Various simplifying assumptions lead to estimates of mass loss rates that differ from one another by many orders of magnitude (Wood, 1979). Therefore, an analysis must be based on the self–consistent solution of the radiation transfer, fluid dynamics and rate equations. Unfortunately, the description of the shock wave passage in terms of the Lagrangean approach cannot be applied since it does not allow the postshock relaxation zones to be explicitly resolved with respect to the spatial coordinate (Klein et al., 1976; Klein et al., 1978). Another approach is based on the assumption of the steady–state gas flow. Applicability of this assumption for shock waves in stellar atmospheres is justified by the small width of the shock wave in comparison with the atmosphere scale height.

Another necessary condition for applicability of the steady–state assumption implies that the characteristic time scale of the shock wave decay is $t_{\rm dec} \ll d/U$, where d and U are the width and velocity of the shock wave. In atmospheres of radially pulsating stars this condition is obviously fulfilled because emission lines indicating the shock wave are observed during the major part of the pulsation period (Abt, 1954; Willson, 1976) and in some stars this interval is as long as a half (Fox et al., 1984) or even 0.8 (Gillet et al., 1985) of the pulsation period.

Even in the framework of the steady–state assumption the problem of the shock wave structure in the partially ionized gases remains tremendously difficult due to the strong coupling between the radiative precursor and the shock wake. Indeed, the occupation number densities of bound and free levels in both atoms and molecules strongly depend on the radiation field produced in the shock wake and at the same time must be determined as a solution of rate equations that are stiff on the relevant time scales. Fortunately, in stars with effective temperatures of $T_{\rm eff} \gtrsim 3000$K the gas is mostly in atomic state and the principal dissipative processes in the postshock region are excitation and ionization of atoms.

In Paper I (Fadeyev & Gillet, 1998) we proposed the method of global iterations that allows us to obtain the stable self–consistent solution of the equations of fluid dynamics, radiation transfer and rate equations for the steady–state plane–parallel shock wave propagating through the atomic hydrogen gas. In Paper II (Fadeyev & Gillet, 2000) this method has been employed for computations of the structure of shocks with upstream velocities of 15 km s^{-1} $\le U_1 \le$ 70 km s^{-1} and for the temperature and the density of the unperturbed hydrogen gas of $T_1 = 6000$K and $\rho_1 = 10^{-10}$ gm cm^{-3}, respectively. Results of these calculations are obviously insufficient for astrophysical applications since the temperature and the density in atmospheres of pulsating stars vary in wide ranges.

Below we discuss the structure of shock waves propagating through the partially ionized hydrogen gas with temperature and density ranged within $3000\text{K} \le T_1 \le 8000\text{K}$ and 10^{-12} gm cm^{-3} $\le \rho_1 \le 10^{-9}$ gm cm^{-3}, respectively. Basic equations and the method of their solution are described in Paper II. In comparison with our previous work we improved the treatment of the radiation transfer and extended the total spectral range to $13 \le \log\nu \le 16$. All calculations were done for the hydrogen atom with $L = 4$ bound levels and a continuum.

2. General description of the shock wave structure

In the comoving fluid frame the radiation–modified Rankine–Hugoniot relations are written (Marshak, 1958; Mihalas & Weibel Mihalas, 1984) as

$$\rho U = \mathcal{C}_0 \equiv \dot{m}, \tag{1}$$

$$\dot{m}U + P_{\rm g} + P_{\rm R} = \mathcal{C}_1, \tag{2}$$

$$\frac{1}{2}\dot{m}U^2 + \dot{m}h + F_{\rm R} + U\left(E_{\rm R} + P_{\rm R}\right) = \mathcal{C}_2, \tag{3}$$

where ρ is the gas density, U is the gas flow velocity, h is the specific enthalpy, $P_{\rm g}$ is the gas pressure, $E_{\rm R}$, $F_{\rm R}$ and $P_{\rm R}$ are the radiation energy density, radiation flux and radiation pressure, respectively.

In planar geometry the total energy flux $\mathcal{C}_2$ given by relation (3) is constant along the spatial coordinate X, so that while the parcell of gas passes the shock wave the decrease of the flux of kinetic energy $F_{\rm K} = \frac{1}{2}\dot{m}U^2$ is balanced by changes of the enthalpy flux $F_{\rm h} = \dot{m}h$ and the radiation flux $F_{\rm R}$. Throughout the shock wave the flux $U(E_{\rm R}+P_{\rm R})$ is significantly smaller than other terms of the left–hand side of relation (3) and can be ignored.

As in Paper II the shock wave model is represented by the comoving plane–parallel finite slab. The space coordinate $X = 0$ is set at the viscous adiabatic jump which is treated as an infinitesimally thin discontinuous jump where hydrodynamic variables undergo an abrupt change. It is assumed that the space coordinate X of the gas element increases while the gas flows through the shock wave, so that in the preshock region $X < 0$ and in the postshock region $X > 0$. The coordinates of the preshock and postshock outer boundaries are denoted as X_1 and X_N, respectively. The upstream radiation flux emerging from the preshock outer boundary is negative, whereas the downstream radiation flux emerging from the postshock outer boundary is positive, that is, $F_{\rm R1} < 0$ and $F_{{\rm R}N} > 0$.

On the upper panel of Fig. 1 are shown the fluxes $F_{\rm K}$, $F_{\rm h}$ and $F_{\rm R}$ as a function of space coordinate X for the shock wave model with $\rho_1 = 10^{-10}$ gm cm^{-3}, $T_1 = 6000$K and $U_1 = 60$ km s^{-1}. For the sake of convenience we use the logarithmic scale along the spatial coordinate X, the preshock and postshock regions being represented by the left plot and the right plot, respectively. Below the upper panel of Fig. 1 we show as a function of X the fractional number density of hydrogen atoms in 2–nd state $n_2/n_{\rm H}$, the hydrogen ionization degree $x_{\rm H} = n_{\rm e}/n_{\rm H}$, the electron temperature $T_{\rm e}$ and the temperature of heavy particles (i.e. of neutral hydrogen atoms and hydrogen ions) T_a, and on the lower panel we give the plot of the compression ratio ρ/ρ_1.

We assume that at the preshock outer boundary X_1 the gas temperature and the gas density are the same as those of the unpertubed medium that are denoted as T_1

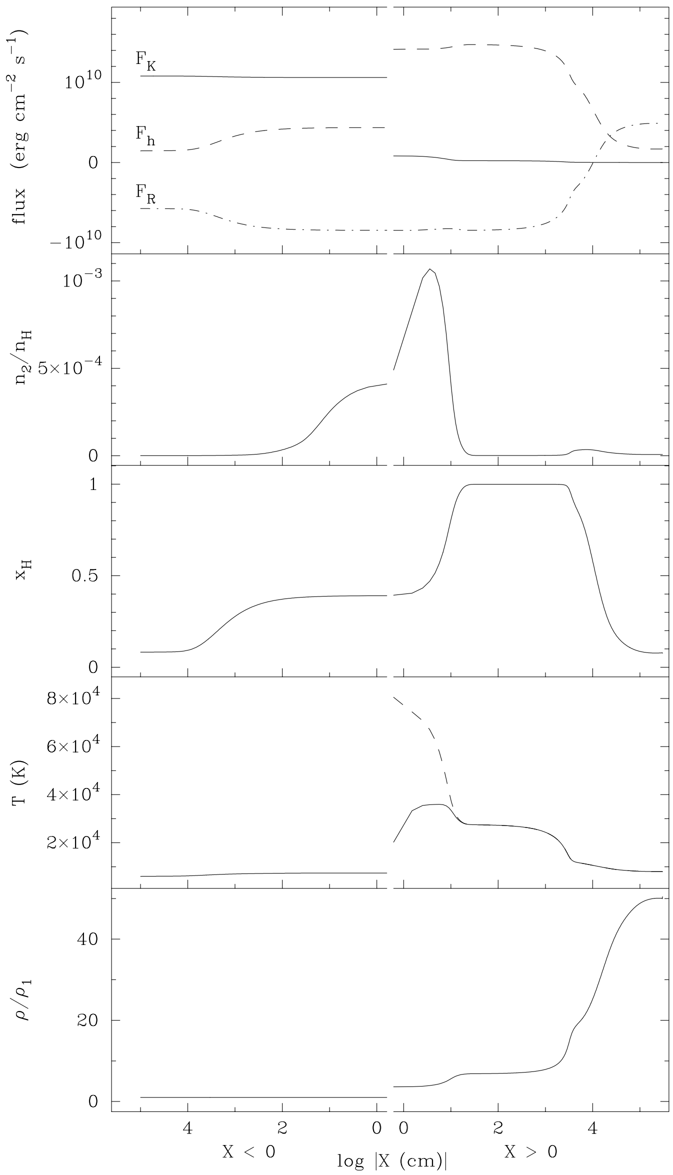

Fig. 1. The structure of the shock wave with $\rho_1 = 10^{-10}$ gm cm^{-3}, $T_1 = 6000$K and $U_1 = 60$ km s^{-1}. On the upper panel the solid lines, dashed lines and dot–dashed lines represent the flux of the kinetic energy $F_{\rm K}$, the flux of the enthalpy $F_{\rm h}$ and the radiation flux $F_{\rm R}$. On lower panels are given the fractional number density of hydrogen atoms in 2–nd state $n_2/n_{\rm H}$, the hydrogen ionization degree $x_{\rm H}$, the electron temperature $T_{\rm e}$ (solid lines) and the temperature of heavy particles T_a (dashed line), and the compression ratio ρ/ρ_1.

and ρ_1, respectively. At the same time the upstream radiation flux emerging from the shock wake affects both the bound–level number densities and the ionization degree of hydrogen atoms. Therefore, the number densities of hydrogen atoms in i–th state n_i and the number density of free electrons $n_{\rm e}$ at the preshock outer boundary are determined from the solution of the equations of statistical equilibrium. In our calculations we tried to set the preshock outer boundary X_1 as far as possible from the discontinuous jump in order to diminish the perturbing influence of the shock wave radiation field on the preshock gas.

The most prominent changes that the gas flow undergoes in the preshock region are due to the absorption of the Lyman continuum radiation. In Fig. 1 the radiative precursor is revealed by the growth of the enthalpy flux $F_{\rm h}$ and due to the corresponding changes of the radiation flux $F_{\rm R}$. The length of the radiative precursor $\delta X_{\rm p}$ is proportional to the mean free path of Lyman continuum photons and increases with decreasing density from $\delta X_{\rm p} \sim 10^3$ cm at $\rho_1 = 10^{-9}$ gm cm^{-3} to $\delta X_{\rm p} \sim 10^7$ cm at $\rho_1 = 10^{-12}$ gm cm^{-3}.

Within the radiative precursor the divergence of the Lyman continuum flux is negative, that is,

$$\nabla \cdot \mathbf{F}_{\rm Lyc} = 4\pi \int\limits_{\nu_1}^{\infty} (\eta_\nu - \kappa_\nu J_\nu)\, d\nu < 0, \qquad (4)$$

where η_ν and κ_ν are the monochromatic emission and absorption coefficients, J_ν is the mean intensity, ν_1 is the threshold frequency for ionization from the ground state of the hydrogen atom. Thus, the gas temperature increases due to absorption of the Lyman continuum radiation while the gas parcell approaches the discontinuous jump. As a result, the gas density ρ just ahead the discontinuity exceeds its unperturbed value ρ_1, whereas the gas flow velocity U becomes smaller than U_1. The change of the gas density ρ and the gas flow velocity U in the radiative precursor depends not only on the upstream velocity U_1 but also on the temperature and density of the unperturbed preshock gas. At $\rho_1 = 10^{-10}$ gm cm^{-3} and $U_1 = 75$ km s^{-1} the relative growth of the density within the radiative precursor ranges from $\Delta\rho/\rho_1 \approx 0.03$ at $T_1 = 3000$K to $\Delta\rho/\rho_1 \approx 0.07$ at $T_1 = 7000$K.

It should be noted that when the hydrogen gas is not completely ionized in the preshock region, the increase of the enthalpy flux is mostly due to ionization of hydrogen atoms. The rates of collisional transitions both bound–bound and bound–free are negligible in comparison with those of radiative transitions, so that the increase of $F_{\rm h}$ ahead the discontinuous jump results mostly from the photoionization of hydrogen atoms.

Across the discontinuity the flux of the kinetic energy $F_{\rm K}$ undergoes an abrupt decrease which is exactly balanced by the same abrupt increase of the enthalpy flux $F_{\rm h}$. Because population number densities per unit mass n_i/ρ and $n_{\rm e}/\rho$ do not change across the discontinuity, the rise of the specific enthalpy is only due to the abrupt increase of the temperature of heavy particles T_a and the electron temperature $T_{\rm e}$. Here we assume that the temperature of heavy particles just behind the discontinuous jump is given by the solution of the Rankine–Hugoniot relations (1) – (3):

$$\begin{aligned} T_a^+ \;=\; & T_a^- - x_{\rm H}^-\left(T_{\rm e}^+ - T_{\rm e}^-\right) + \frac{1}{5}\frac{\dot{m}U^-}{n_{\rm H}^- k}\frac{\eta^2-1}{\eta^2} - \\ - \; & \frac{2}{5}\frac{F_{\rm R}^+ - F_{\rm R}^-}{n_{\rm H}^- k U^-} - \\ - \; & \frac{2}{5}\frac{(E_{\rm R}^+ + P_{\rm R}^+)\eta^{-1} - (E_{\rm R}^- + P_{\rm R}^-)}{n_{\rm H}^- k}, \end{aligned} \qquad (5)$$

whereas the electron temperature increases due to adiabatic compression:

$$T_{\rm e}^+ = \eta^{\gamma-1} T_{\rm e}^-, \qquad (6)$$

where $\eta = \rho^+/\rho^-$ is the compression ratio across the discontinuous jump, $\gamma = 5/3$ is the ratio of specific heats of the electron gas, and superscripts minus and plus refer the variables defined ahead and behind the discontinuous jump, respectively [1].

The mean free path of photons in the vicinity of the discontinuous jump is several orders of magnitude larger than that of hydrogen atoms and the radiation flux will remain constant to a high order of accuracy even if we take into account the finite thickness of the viscous adiabatic jump. In our calculations the space interval between two adjacent cell centers located ahead and behind the discontinuity was set for all models equal to 1 cm. Thus, last two terms in the right–hand side of (5) can be omitted without lost of accuracy because they consist of the differences of the upstream and downstream values of the radiation energy density, radiation flux and radiation pressure.

Excitation and ionization of hydrogen atoms behind the discontinuity are mostly due to radiative transitions. The time scale of photoexcitation of lower bound levels is comparable with that of the electron temperature growth, whereas the photoionization of hydrogen atoms is much slower and begins with substantial delay. The growth of the hydrogen ionization leads to the small increase of the enthalpy flux and, correspondingly, to the small decrease of the flux of kinetic energy because the radiation flux almost does not change. However the most promiment process accompanying the hydrogen ionization is the increase of the compression ratio ρ/ρ_1. For the model presented in Fig. 1 the compression ratio increases from $\rho/\rho_1 = 3.6$ just behind the discontinuity up to $\rho/\rho_1 = 6.8$ in the layers where the hydrogen ionization reaches its maximum.

At larger distances from the discontinuity the kinetic energy of the gas flow initially stored as the ionization energy of the gas is converted into radiation. In Fig. 1 these layers are revealed as those of remarkable changes of $F_{\rm h}$ and $F_{\rm R}$ accompanied by the growth of the compression ratio ρ/ρ_1. For models considered in the present study the compression ratio reached at the postshock outer boundary ranges within $1 < \rho_N/\rho_1 \lesssim 10^2$ depending mostly on the upstream velocity U_1 and less on the preshock temperature T_1 and preshock density ρ_1.

The large growth of the postshock compression ratio $\eta = \rho/\rho_1$ is due to the ionization of hydrogen gas and its following radiative cooling. In order to roughly estimate the contribution of these effects let us write the energy conservation relation (3) with omitted radiation energy density and radiation pressure terms as

$$\begin{aligned} & \frac{U_1^2}{2} + \tilde{E}_{\rm t1} + \tilde{E}_{\rm in1} + \frac{P_{\rm g1}}{\rho_1} + \frac{F_{\rm R1}}{\dot{m}} = \\ & = \frac{U^2}{2} + \tilde{E}_{\rm t} + \tilde{E}_{\rm in} + \frac{P_{\rm g}}{\rho} + \frac{F_{\rm R}}{\dot{m}}, \end{aligned} \qquad (7)$$

where $\tilde{E}_{\rm t} = \frac{3}{2}(n_{\rm H} + n_{\rm e})kT/\rho$ is the specific energy in the translational degrees of freedom and $\tilde{E}_{\rm in}$ is the specific energy of excitation and ionization of hydrogen atoms. The left–hand side of (7) is written for the preshock outer boundary, whereas its right–hand side represents an arbitrary layer of the postshock region.

Relation (7) and the momentum conservation relation (2) can be rewritten as

$$\eta = 4 + 3\frac{\tilde{E}_{\rm in} - \tilde{E}_{\rm in1}}{\tilde{E}_{\rm t}} + 3\frac{F_{\rm R} - F_{\rm R1}}{\dot{m}\tilde{E}_{\rm t}}, \qquad (8)$$

where we assumed that the specific energy in the translational degrees of freedom of the preshock gas is negligible in comparison with that of the postshock compressed gas, that is, $\tilde{E}_{\rm t1}/\eta \ll \tilde{E}_{\rm t}$.

The first term in the right–hand side of (8) is the limiting compression ratio of the atomic hydrogen gas at the discontinuous jump. The second term in the right–hand side of (8) describes the compression of the postshock gas due to excitation and ionization of hydrogen atoms. For the model shown in Fig. 1 the maximum hydrogen ionization degree is $x_{\rm H} = 0.99$ and the ratio of the specific energies is $\tilde{E}_{\rm in}/\tilde{E}_{\rm t} \approx 2$. Thus, the upper limit for the compression ratio beyond the layers of hydrogen ionization is $\eta \approx 10$.

However the most important contribution into the growth of the compression ratio belongs to the third term in the right–hand side of (7). Indeed, for the model shown in Fig. 1 the ratio of the sum of radiative fluxes (note that $F_{\rm R1}$ is negative) to the flux of the translational energy of the gas at the postshock outer boundary is $(F_{{\rm R}N} - F_{\rm R1})/(\dot{m}\tilde{E}_N) \approx 18$. Therefore, the maximum compression ratio at the postshock outer boundary is $\eta \approx 64$.

3. Effects of the preshock temperature

Just behind the discontinuity the temperature of electrons $T_{\rm e}$ is substantially lower than the temperature of heavy particles T_a and electrons acquire the energy in elastic collisions with neutral hydrogen atoms and hydrogen ions. Because the elastic scattering cross section of electrons and hydrogen ions is much larger than that of electrons

[1] In relation (5) we corrected the typeset errors appeared in relation (15) of Paper II.

and neutral hydrogen atoms, the efficiency of the energy exchange between heavy particles and free electrons is very sensitive to the hydrogen ionization degree $x_{\rm H}^-$ ahead the discontinuous jump. In particular, at $x_{\rm H}^- \gtrsim 10^{-2}$ the postshock equilibration between the electron temperature $T_{\rm e}$ and the temperature of heavy particles T_a is due to elastic scattering of electrons by hydrogen ions and the equilibration rate very rapidly increases with increasing $x_{\rm H}^-$. And, vice versa, at $x_{\rm H} < 10^{-2}$ free electrons gain the most of the energy from elastic collisions with neutral hydrogen atoms and the rate of temperature equilibation is much smaller. This process, however, is perceptible only in shock waves with weak ionization in the radiative precursor (that is, at upstream velocities $U_1 < 30$ km s^{-1}), the preshock gas temperature being of $T_1 < 4000$K.

Thus, effects of the preshock gas temperature on the shock wave structure are mostly due to the preshock equilibrium hydrogen ionization. This is illustrated in Fig. 2 for shock wave models with $T_1 = 4000$K and $T_1 = 8000$K. In both cases the preshock gas density and the upstream velocity are $\rho_1 = 10^{-10}$ gm cm^{-3} and $U_1 = 40$ km s^{-1}, respectively, so that the postshock equilibration of $T_{\rm e}$ and T_a is due to elastic scattering of electrons by hydrogen ions. As is seen from the upper panel of Fig. 2 the hydrogen ionization degree just behind the discontinuous jump is $x_{\rm H} \approx 0.02$ at $T_1 = 4000$K and $x_{\rm H} \approx 0.46$ at $T_1 = 8000$K. As a result, at preshock gas temperature $T_1 = 8000$K the rate of the energy gain by electrons in elastic collisions with hydrogen ions is larger by a factor of 60 than that at $T_1 = 4000$K.

The increase of the preshock gas temperature T_1 is accompanied also by the stronger radiation flux emerging from the shock wave. This is, obviously, due to the higher hydrogen ionization degree in the postshock region. The more gradual changes of the postshock electron temperature and of the ionization degree in shocks with higher preshock temperature lead to smaller compression ratios ρ/ρ_1 (see the lower panel of Fig. 2).

In Fig. 3 we give the plots of the final compression ratio ρ_N/ρ_1 which is reached at the postshock outer boundary X_N in shock wave models with $\rho_1 = 10^{-10}$ gm cm^{-3}. It should be noted that the final postshock gas density asymptotically tends to its limiting value ρ_∞ with $X \to \infty$ and because in our study the shock wave model is represented by the finite slab, the compression ratio ρ_N/ρ_1 gives only the lower estimate for the limiting value ρ_∞/ρ_1. In our calculations we tried to set the postshock outer boundary as far as possible from the discontinuous jump. Unfortunately, the convergence of global iterations is very sensitive to the spatial coordinate of the postshock outer boundary and for too large X_N iterations diverge. Thus, the coordinate X_N was determined for each model from trial calculations as a compromise between requirements to treat the major part of the postshock region and demands of the convergence and accuracy. That is why the

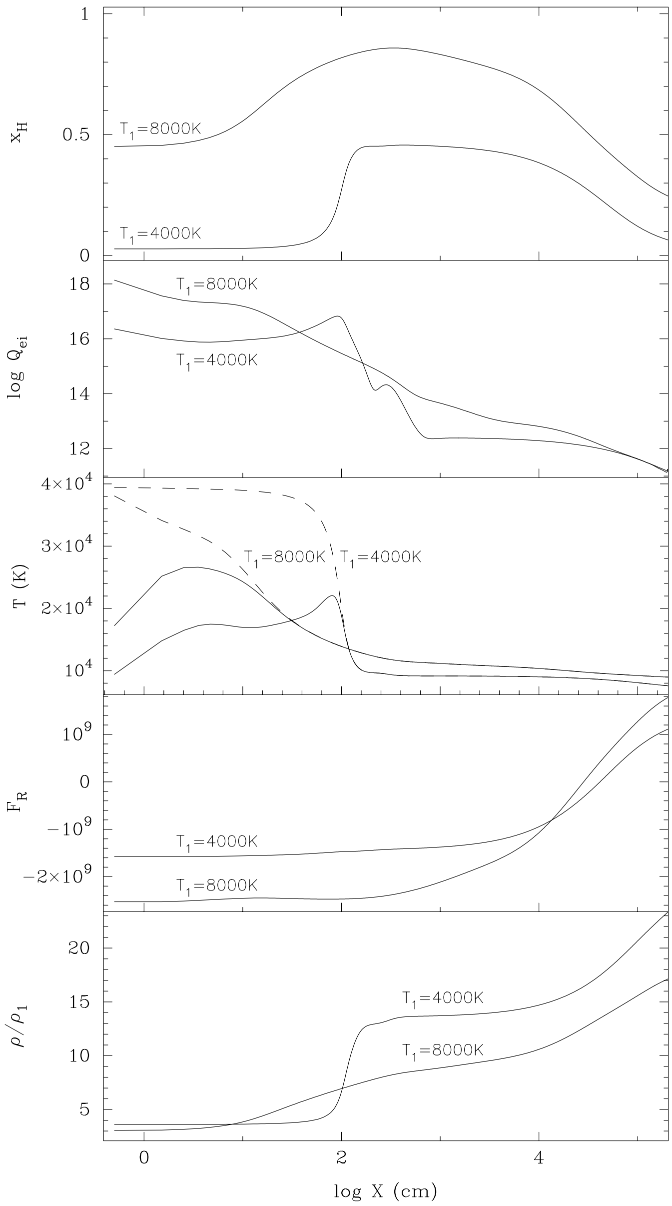

Fig. 2. The postshock hydrogen ionization degree $x_{\rm H}$, the rate of energy gain by electrons in elastic collisions with hydrogen ions per unit mass $Q_{\rm ei}$, the electron temperature $T_{\rm e}$ (solid lines) and the temperature of heavy particles T_a (dashed lines); the radiation flux $F_{\rm R}$ and the compression ratio ρ/ρ_1 as a function of distance from the discontinuous jump in shock wave models with $\rho_1 = 10^{-10}$ gm cm^{-3}, $U_1 = 40$ km s^{-1}, $T_1 = 4000$K and $T_1 = 8000$K.

filled circles in Fig. 3 representing the models with the same value of T_1 are not on the smooth curves.

At fixed upstream velocity U_1 the Mach number $M_1 = U_1/a_1$ decreases with increasing T_1 due to the temperature dependence of the adiabatic sound speed a_1 at the preshock outer boundary. In the hydrogen gas with negligible ionization ($\rho_1 = 10^{-10}$ gm cm^{-3}, $T_1 \lesssim 7000$K) the adiabatic sound speed is $a_1 \propto \sqrt{T_1}$ and the compression

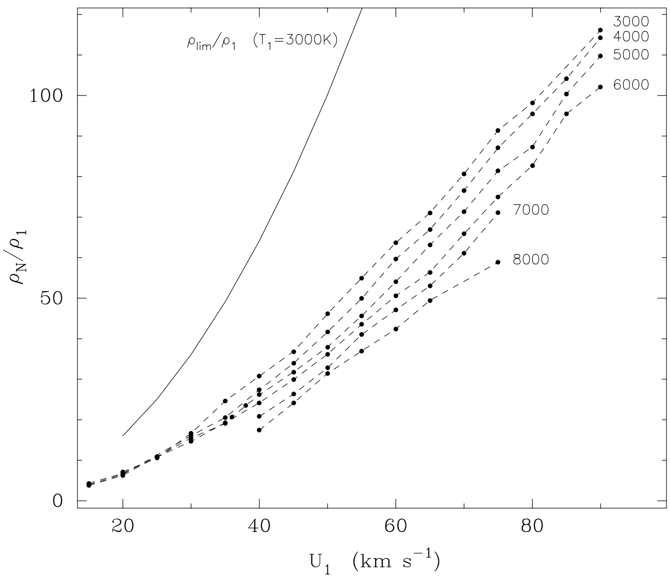

Fig. 3. The compression ratio ρ_N/ρ_1 at the postshock outer boundary as a function of upstream velocity U_1 at $\rho_1 = 10^{-10}$ gm cm^{-3} and 3000K $\le T_1 \le$ 7000K. Each sequence of models with the same preshock temperature T_1 is represented by filled circles connected by dashed lines. Each curve is labeled with T_1. In solid line is shown the compression ratio of the isothermal shock wave propagating through the gas with $T_1 = 3000$K.

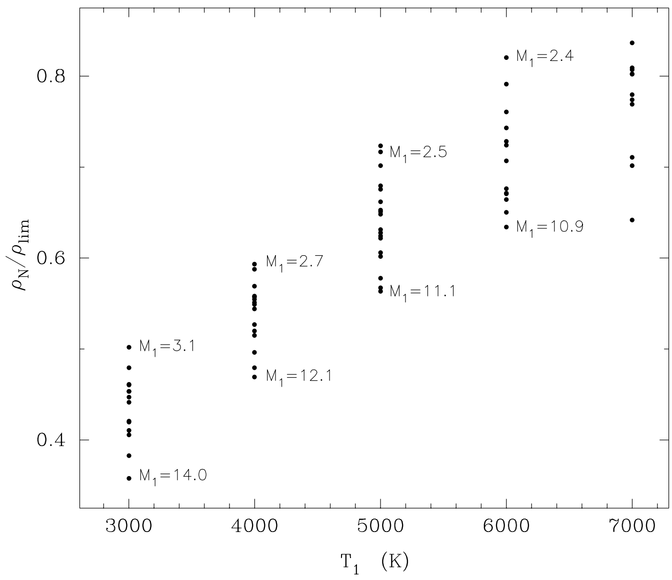

Fig. 4. The final compression ratio ρ_N/ρ_1 at the postshock outer boundary in units of the compression ratio of the isothermal shock wave $\rho_{\rm lim}/\rho_1$ versus the preshock gas temperature T_1 for models with $\rho_1 = 10^{-10}$ gm cm^{-3} and 20 km s^{-1} $\le U_1 \le$ 90 km s^{-1}. At fixed preshock temperature T_1 the values of the Mach number M_1 correspond to models with $U_1 = 20$ km s^{-1} and $U_1 = 90$ km s^{-1}, respectively.

ratio

$$\rho_{\rm lim}/\rho_1 = \gamma M_1^2 \tag{9}$$

corresponding to the isothermal shock wave is inversly proportional to T_1. On the other hand, as is seen from Fig. 3, the final compression ratio ρ_N/ρ_1 at the postshock outer boundary also decreases with increasing preshock temperature though this dependence is not so prominent as that of $\rho_{\rm lim}/\rho_1$.

In Fig. 4 we show the ratio $\rho_N/\rho_{\rm lim}$ for shock wave models with $\rho_1 = 10^{-10}$ gm cm^{-3}, 3000K $\le T_1 \le$ 7000K, 20 km s^{-1} $\le U_1 \le$ 90 km s^{-1}. Each model on this plot is represented by the filled circle and for models with with $U_1 = 20$ km s^{-1} and $U_1 = 90$ km s^{-1} we give the values of the upstream Mach number M_1.

At fixed preshock gas temperature T_1 the ratio $\rho_N/\rho_{\rm lim}$ decreases with increasing upstream velocity since the final compression ratio ρ_N/ρ_1 grows with U_1 slower than $\rho_{\rm lim}/\rho_1$ (compare dependencies of ρ_N/ρ_1 and $\rho_{\rm lim}/\rho_1$ shown for $T_1 = 3000$K in Fig. 3). However the most interesting feature is that the increase of the preshock gas temperature T_1 is accompanied by the gradual approach of the final compression ratio ρ_N/ρ_1 to its upper limit $\rho_{\rm lim}/\rho_1$ corresponding to the isothermal shock wave. This is due to the decrease of the Mach number M_1 with increasing T_1.

4. Effects of the preshock density

Two upper panels of Fig. 5 show the postshock hydrogen ionization degree $x_{\rm H}$ and the postshock temperatures $T_{\rm e}$ and T_a as a function of distance from the discontinuous jump for shock wave models with 10^{-12} gm cm^{-3} $\le \rho_1 \le$ 10^{-9} gm cm^{-3}, $T_1 = 6000$K and $U_1 = 50$ km s^{-1}. On two lower panels of Fig. 5 for the same models are shown the radiation flux $F_{\rm R}$ and the compression ratio ρ/ρ_1. It should be noted that for better graphical representation we use the logatithmic scale for the plot of radiative flux and the deep minima of $\log|F_{\rm R}|$ correspond to layers with $F_{\rm R} \approx 0$.

The main results of these calculations are as follows. First, the width of the postshock relaxation zone increases with decreasing preshock gas density ρ_1. This is due to the fact that the mean collision time of particles is proportional to the gas density. Second, the radiative flux produced by the shock wave decreases with decreasing ρ_1 because the kinetic energy of the gas flow at the preshock outer boundary is proportional to ρ_1. Third, more gradual ionization and recombination of hydrogen atoms at lower preshock gas density ρ_1 lead to smaller postshock compression ratios.

5. Radiative flux of the shock wave

As is seen from plots on the upper panel of Fig. 1 the upstream radiative flux $F_{\rm R1}$ emerging from the preshock outer boundary and the downstream radiation flux $F_{{\rm R}N}$

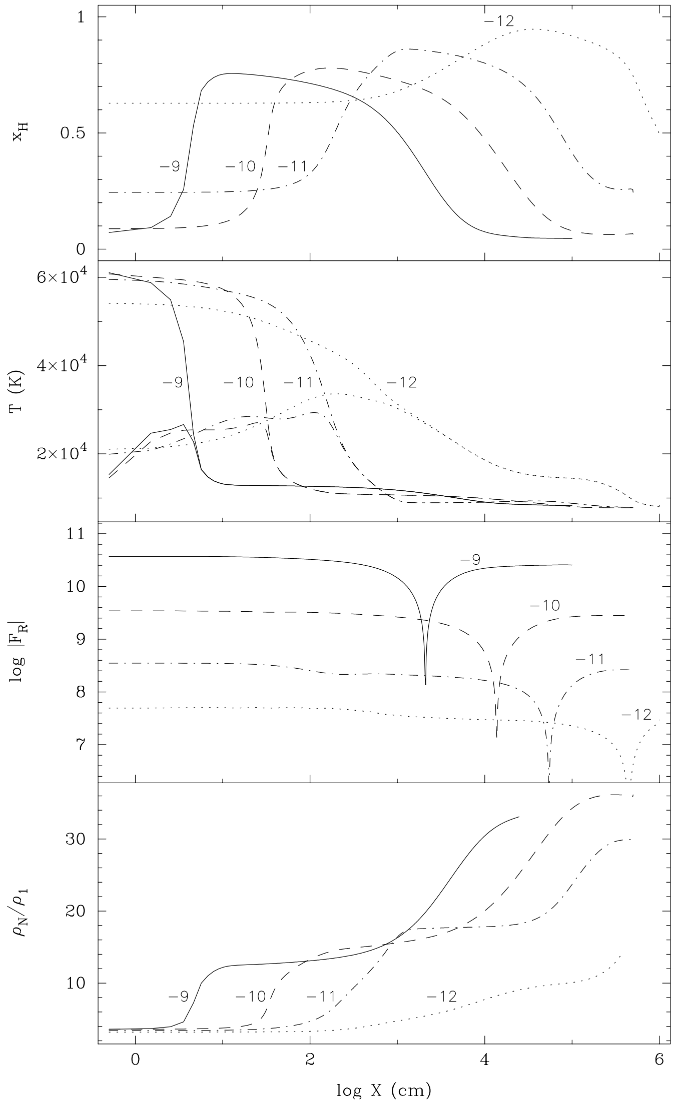

Fig. 5. The hydrogen ionization degree $x_{\rm H}$, the electron temperature $T_{\rm e}$ and the temperature of heavy particles T_a, the radiation flux $F_{\rm R}$ and the compression ratio ρ/ρ_1 as a function of distance from the discontinuous jump in the postshock region at $T_1 = 6000$K and $U_1 = 50$ km s^{-1}. In solid, dashed, dot–dashed and dotted lines are shown the dependencies corresponding to the preshock gas density $\rho_1 = 10^{-9}$, 10^{-10}, 10^{-11} and 10^{-12} gm cm^{-3}, respectively. Each curve is labeled with $\log\rho_1$.

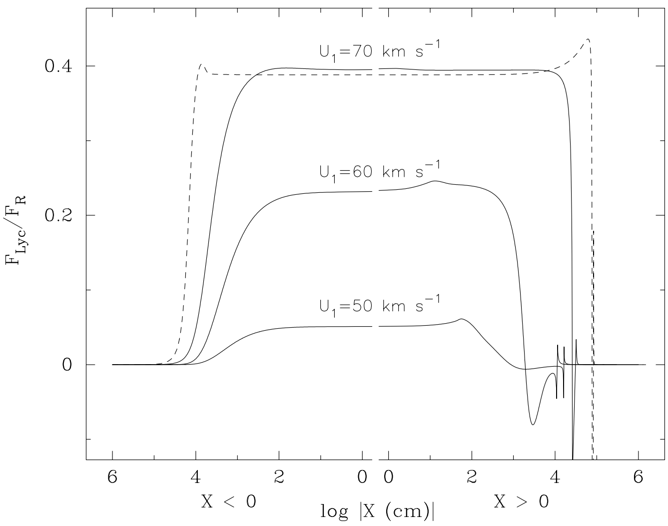

Fig. 6. The ratio of the radiation flux in the Lyman continuum to the total radiation flux $F_{\rm Lyc}/F_{\rm R}$ in vicinity of the discontinuous jump of shock waves with upstream velocity $U_1 = 50$, 60, 70 (solid lines) and 80 km s^{-1} (dashed line).

emerging in opposite direction from the postshock outer boundary are not equal by absolute value. This difference increases with increasing upstream velocity. For example, at $\rho_1 = 10^{-10}$ gm cm^{-3} and $T_1 = 6000$K the ratio of these fluxes ranges from $|F_{\rm R1}|/F_{{\rm R}N} \approx 1.01$ at $U_1 = 20$ km s^{-1} to $|F_{\rm R1}|/F_{{\rm R}N} \approx 1.16$ at $U_1 = 60$ km s^{-1}.

However the much stronger asymmetry of the radiation field is revealed at frequencies $\nu > \nu_1$ because the Lyman continuum flux is directed mostly upstream. The region of the effective transport of the Lyman continuum radiation encompasses the near vicinity of the discontinuous jump. Ahead the discontinuity this is the radiative precursor and behind the discontinuity the Lyman continuum flux becomes negligible where the total radiation flux changes its sign, that is in the layers with $F_{\rm R} \approx 0$. The contribution of the Lyman continuum into the total radiation flux within this region rapidly increases with increasing upstream velocity. For example, for shock waves propagating in the gas with $\rho_1 = 10^{-10}$ gm cm^{-3} and $T_1 = 3000$K the ratio of the Lyman continuum flux to the total radiation flux increases from $F_{\rm Lyc}/F_{\rm R} \approx 10^{-2}$ at $U_1 = 40$ km s^{-1} to $F_{\rm Lyc}/F_{\rm R} \approx 0.2$ at $U_1 = 60$ km s^{-1}. The growth of the ratio $F_{\rm Lyc}/F_{\rm R}$ ceases at upstream velocity $U_1 \approx 75$ km s^{-1} corresponding to almost full hydrogen ionization in the radiative precursor. At larger upstream velocities the fraction of the Lyman continuum radiation does not exceed $\approx 40\%$ of the total radiation flux but the region of the effective transport of the Lyman continuum radiation becomes wider both ahead and behind the discontinuity.

The plots of the ratio $F_{\rm Lyc}/F_{\rm R}$ for shock wave models with upstream velocities 50 km s^{-1} $\le U_1 \le$ 80 km s^{-1} are shown in Fig. 6. It should be noted that the positive value of the ratio $F_{\rm Lyc}/F_{\rm R}$ implies that the total radiation flux and the Lyman continuum flux are both negative and are directed upstream. Negative values of this ratio imply that the Lyman continuum flux is directed downstream whereas the total radiation flux is still upstream. Oscillations of the ratio $F_{\rm Lyc}/F_{\rm R}$ in the postshock region are due to vanishing values of $F_{\rm R}$.

Thus, behind the discontinuous jump the Lyman continuum flux $F_{\rm Lyc}$ changes its sign at smaller distance than

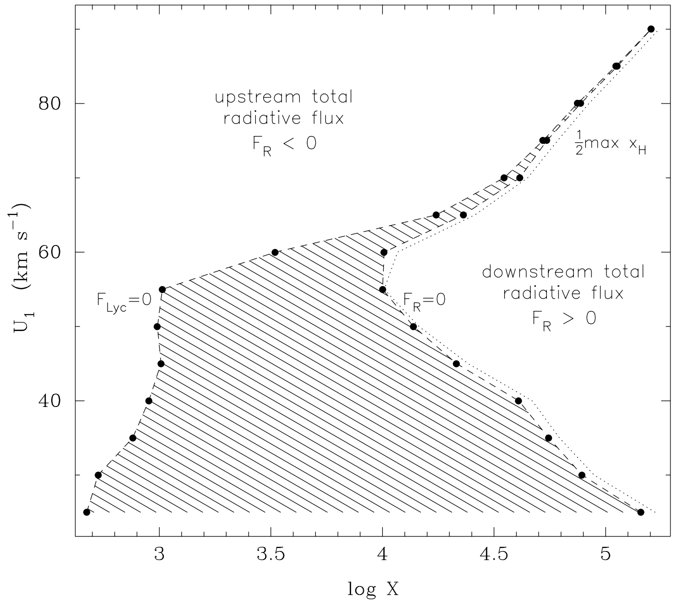

Fig. 7. The zones of upstream ($F_{\rm R} < 0$) and downstream ($F_{\rm R} > 0$) total riadiave flux in the postshock region at $\rho_1 = 10^{-10}$ gm cm^{-3} and $T_1 = 6000$K. The shaded area represents the zone with downstream Lyman continuum flux and upstream flux $F(\nu < \nu_1)$. The dotted curve marked $\frac{1}{2}\max x_{\rm H}$ gives the locus where the hydrogen ionization degree is a half of its maximum postshock value.

the radiative flux

$$F(\nu < \nu_1) = \int_0^{\nu_1} F_\nu d\nu \qquad (10)$$

transported at frequencies below the Lyman continuum edge ν_1. In Fig. 7 we depict the diagram representing the zones of the postshock region with upstream and downstream total radiative flux $F_{\rm R}$ in shock wave models with $\rho_1 = 10^{-10}$ gm cm^{-3} and $T_1 = 6000$K. The zone with downstream Lyman continuum flux ($F_{\rm Lyc} > 0$) and upstream flux $F(\nu < \nu_1)$ is shown on this diagram by the shaded area. Space coordinates $X[F(\nu < \nu_1) = 0]$ and $X(F_{\rm R} = 0)$ coincide because the most of radiation is transported in these layers at frequencies below the Lyman continuum edge.

In Fig. 7 we show also the space coordinates of the layers where a half of the ionized hydrogen atoms is recombined. The close values of $X(F_{\rm R} = 0)$ and $X(\frac{1}{2}\max x_{\rm H})$ clearly illustrate that the main mechanism of the shock wave energy dissipation is the ionization of hydrogen atoms.

At upstream velocity $U_1 < 60$ km s^{-1} the postshock gas remains partially ionized and the maximum ionization degree increases with increasing U_1 while the space coordinate of the ionization maximum decreases. Correspondingly, the hydrogen recombination also occurs at smaller distance from the discontinuous jump.

At upstream velocity $U_1 > 60$ km s^{-1} the hydrogen is fully ionized and the width of the zone with $x_{\rm H} \approx 1$ increases with increasing U_1. Correspondingly, the hydrogen recombines at larger distances from the discontinuous jump and the coordinate $X(F_{\rm R} = 0)$ increases with increasing U_1. At full hydrogen ionization the zone of the effective energy transport in the Lyman continuum spreads both upstream and downstream with increasing upstream velocity and at $U_1 > 80$ km s^{-1} both the Lyman continuum flux and the total radiation flux change the sign nearly in the same layers.

Another interesting conclusion which follows from the diagram in Fig. 7 is that the width of shock waves with partial postshock hydrogen ionization decreases with increasing upstream velocity U_1, whereas the width of shock waves with full postshock hydrogen ionization increases with increasing upstream velocity.

6. Frequency dependent radiation field

The radiation field produced by the shock wave is remarkably non–equilibrium and any attempts to use an assumption of the thermal equilibrium inevitably lead to large errors. In order to evaluate the degree of departure from thermal equilibrium it is instructive to compare the monochromatic mean intensity J_ν with the local Planck function $B_\nu(T_{\rm e})$. In Fig. 8 the plots of J_ν and $B_\nu(T_{\rm e})$ are shown as a function of frequency ν for four distinct layers of the shock wave model with $\rho = 10^{-10}$ gm cm^{-3}, $T_1 = 6000$K and $U_1 = 60$ km s^{-1}. For the sake of convenience each pair of plots is shifted with respect to others.

The upper pair of plots represent J_ν and $B_\nu(T_{\rm e})$ at $X \approx 10^4$ cm. As is seen from Fig. 1 the photoionization of hydrogen atoms in these layers due to absorption of the Lyman continuum radiation becomes perceptible and this layer can be roughly considered as the boundary of the radiative precursor. Excess of radiation in comparison with $B_\nu(T_{\rm e})$ at frequencies $\nu > \nu_1$ is due to the fact that the optical depth of the radiative precursor decreases with increasing frequency ν.

The second and the third pairs of plots represent the cell just behind the discontinuous jump ($X = 0.5$ cm) and the layer where the hydrogen ionization degree reaches its maximum ($X \approx 40$ cm). Between these layers various relaxation processes redistribute the energy of heavy particles among other degrees of freedom and the radiation field is most non–equilibrium.

The lower pair of plots represent the layers ($X \approx 1.2 \cdot 10^5$ cm) where most of the hydrogen atoms are recombined and the gas temperature gradually approaches its unperturbed value T_1. The optical depth at frequencies of the Lyman continuum is so large that J_ν and $B_\nu(T_{\rm e})$ coincide at $\nu > \nu_1$.

All shock wave models demonstrate two common features. First, the excess of the Lyman continuum radiation in the preshock region due to the existence of the radiative

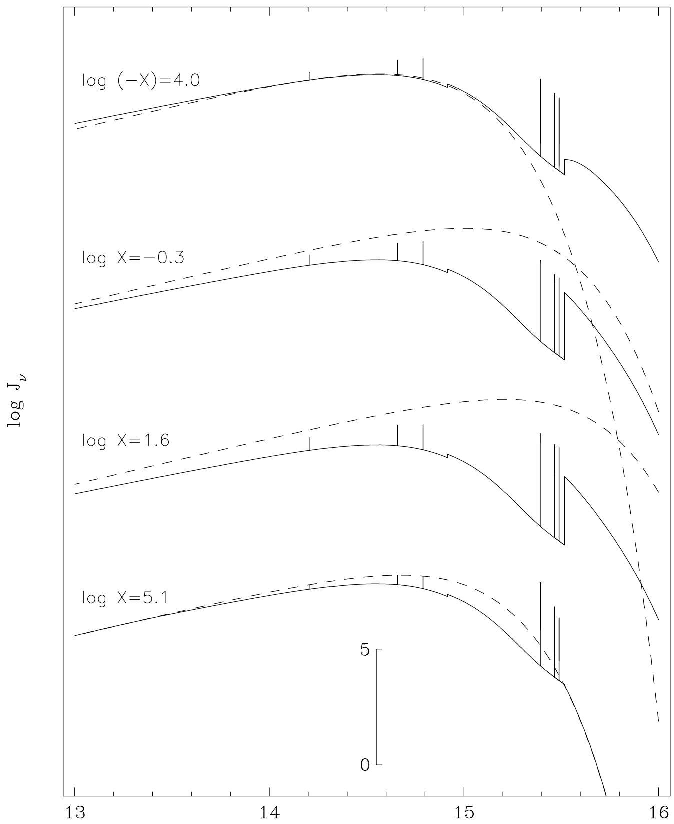

Fig. 8. Monochromatic mean intensity J_ν (solid lines) and the local Planck function $B_\nu(T_e)$ (dashed lines) as a function of frequency ν for four distinct layers of the shock wave with $\rho = 10^{-10}$ gm cm^{-3}, $T_1 = 6000$K and $U_1 = 60$ km s^{-1}. The upper pair of plots represent the preshock region, whereas other plots represent the postshock region.

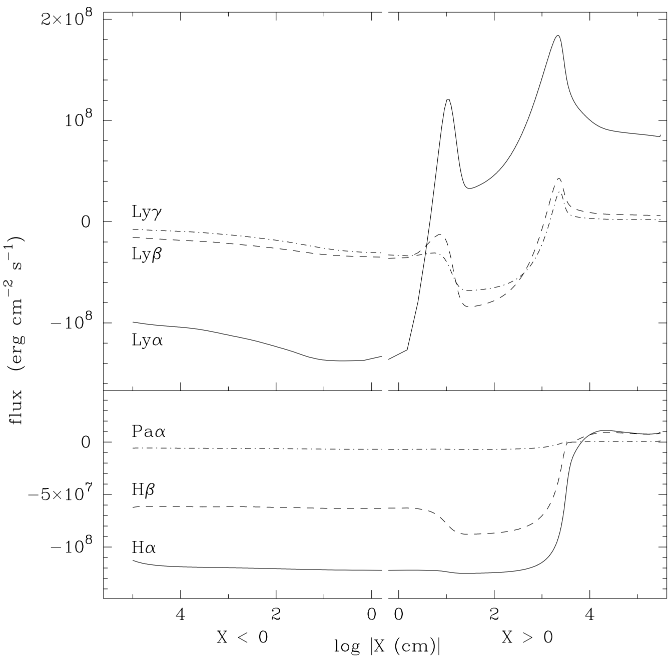

Fig. 9. The radiation flux integrated over spectral line frequency intervals as a function of space coordinate X for the shock wave model with $\rho_1 = 10^{-10}$ gm cm^{-3}, $T_1 = 6000$K and $U_1 = 60$ km s^{-1}.

precursor. Second, the lower mean intensity J_ν in comparison with $B_\nu(T_e)$ due to the small optical depth of the shock wave at frequencies $\nu < \nu_1$.

The plots of the mean intensity J_ν displayed in Fig. 8 reveal the presence of six spectral line features. These are Lyα, Lyβ, Lyγ, Hα, Hβ and Paα. In comparison with our previous work described in Paper II we improved the treatment of the spectral line radiation transfer and considered each line of frequency ν_0 within the frequency interval as wide as $[\nu_0(1-\delta), \nu_0(1+\delta)]$, where $\delta = 5 \cdot 10^{-4}$. The use of wide frequency intervals is necessary because of the strong Doppler broadening of line profiles behind the discontinuous jump. In particular, the radiation flux transported in spectral lines is not negligible and contribution of the spectral line radiation into the total radiation flux increases with increasing upstream velocity. The most important are the Lyα and Hα lines. For example, in the shock wave model with $\rho_1 = 10^{-10}$ gm cm^{-3}, $T_1 = 6000$K and $U_1 = 60$ km s^{-1} the upstream radiation flux in Lyα and Hα lines emerging from the preshock outer boundary is $\approx 2\%$ of the total radiation flux.

In Fig. 9 we show the plots of the radiation flux integrated within frequency intervals of Lyα, Lyβ, Lyγ (upper panel), Hα, Hβ and Paα (lower panel) lines. Comparing with plots of $n_2/n_{\rm H}$ and $x_{\rm H}$ displayed in Fig. 1 we can conclude that the spectral line radiation is produced mostly in the layers of hydrogen recombination. Another interesting feature is that the upstream and downstream Lyα radiation fluxes are nearly equal by absolute value, whereas the radiation flux in Balmer lines emerges mostly upstream.

7. Radiative losses of the shock wave

In order to estimate the irreversible losses of the shock wave energy it is instructive to compare the values of each term of the left–hand side of relation (3) at both boundaries of the slab. In Fig. 10 these quantities are shown for shock wave models with $\rho_1 = 10^{-10}$ gm cm^{-3}, $T_1 = 6000$K and 20 km s^{-1} $\le U_1 \le$ 80 km s^{-1}. As is seen from comparison of the upper and lower panels representing the preshock and postshock outer boundaries, respectively, the most of the kinetic energy of the gas flow is irreversibly lost since the ratio of the fluxes of kinetic energy at both boundaries of the slab ranges within $10^2 \lesssim F_{\rm K1}/F_{{\rm K}N} \lesssim 7 \cdot 10^3$. At the same time the increase of the enthalpy flux after the passage of the parcell of gas through the slab does not exceed 20%. Thus, most of the energy of the shock wave is lost due to radiation.

The role of radiation in irreversible energy losses of the shock wave can be evaluated from comparison of the radiation flux emerging from the boundary of the slab with

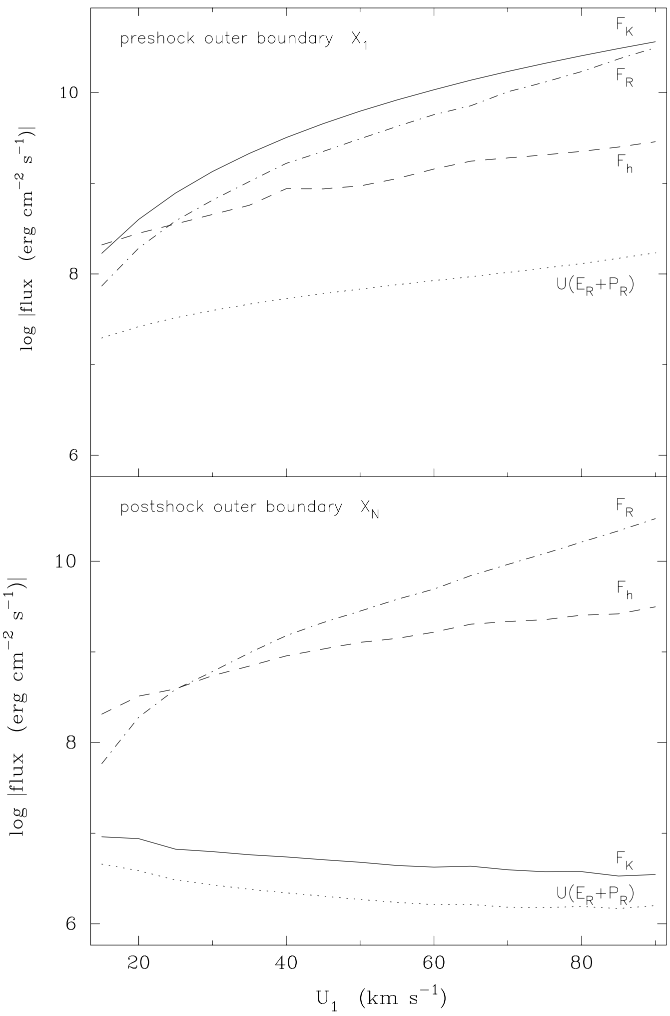

Fig. 10. The flux of kinetic energy $F_{\rm K}$ (solid lines), the flux of enthalpy $F_{\rm h}$ (dashed lines), the radiation flux $F_{\rm R}$ (dot–dashed lines), and the flux $U(E_{\rm R}+P_{\rm R})$ (dotted lines) at the preshock (upper panel) and postshock (lower panel) outer boundaries of the slab as a function of upstream velocity U_1 in the models with $\rho_1 = 10^{-10}$ gm cm^{-3} and $T_1 = 6000$K.

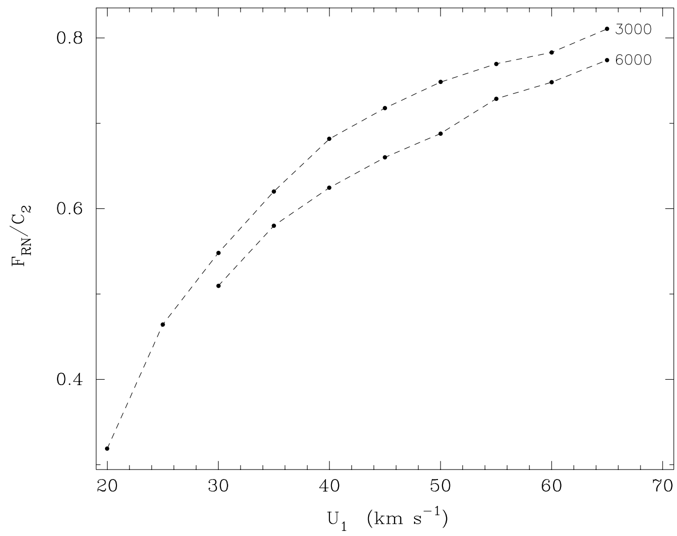

Fig. 11. The ratio of the downstream radiation flux to the total energy flux $F_{{\rm R}N}/\mathcal{C}_2$ at the postshock outer boundary as a function of upstream velocity U_1 for shock wave models with $\rho_1 = 10^{-10}$ gm cm^{-3}. Each curve is labeled with T_1.

the total energy flux $\mathcal{C}_2$. In Fig. 11 the plots of the ratio $F_{{\rm R}N}/\mathcal{C}_2$ at the postshock outer boundary are shown for two sequences of shock wave models with $T_1 = 3000$K and $T_1 = 6000$K. As is seen, the radiative losses increase very rapidly with increasing upstream velocity U_1, though there is also the dependence on the preshock gas temperature T_1.

8. Conclusion

In this work we improved the treatment of the radiation transfer and considered the structure of shock waves propagating through the partially ionized hydrogen gas with density ranged from 10^{-12} gm cm^{-3} to 10^{-9} gm cm^{-3}. Our calculations have shown that while the unpertubed hydrogen gas is partially ionized, the preshock gas temperature affects the shock wave structure mostly due to the preshock hydrogen ionization because the postshock equilibration of translational degrees of freedom is very sensitive to the number density of hydrogen ions. In general, the higher temperature of the preshock gas leads to the larger postshock ionization and to the stronger radiation field produced by the shock wave. At the same time, the increase of the preshock gas temperature is accompanied by the slight decrease of the postshock gas compression.

The preshock gas density ρ_1 affects the shock wave structure mostly due to the fact that the preshock flux of kinetic energy as well as the radiation flux emerging from the shock wave are proportional to ρ_1. Therefore, in the gas with lower density the shock wave produces the weaker radiation flux and the smaller compression of the postshock gas.

The increase of the shock wave velocity leads to higher rates of relaxation processes in the compressed gas behind the discontinuous jump and to the higher postshock ionization. While the maximum ionization degree of the postshock gas is less than unit, the width of the shock wave decreases with increasing shock wave velocity. However, when the postshock gas is fully ionized, the increase of the shock wave velocity leads to the extension of the postshock zone of hydrogen ionization and, therefore, to the increase of the shock wave width.

Strong radiative cooling of the postshock gas leads to compression ratios as high as $\rho/\rho_1 \sim 10^2$. So large increase of the postshock gas density obviously can favour the condensation of dust grains in outer atmospheres of radially pulsating late–type giants.

The isothermal approximation undoubtedly overestimates the radiative losses of the shock wave energy by at least a factor of two for shocks with upstream velocity of $U_1 \lesssim 30\ \mathrm{km\,s^{-1}}$ and can provide a good accuracy at upstream velocities of $U_1 > 80\ \mathrm{km\,s^{-1}}$, that is at Mach numbers $M_1 \gtrsim 10$.

Our calculations demonstrated that the monocromatic radiation flux at frequencies of hydrogen lines significantly exceeds the flux of the background continuum, so that our models reproduce the emission spectrum observed in radially pulsating late–type supergiants. Moreover, the fraction of the energy transported in hydrogen lines is not negligible and can be as large as one or two percent of the total radiation flux because of the strong broadening of the line profiles behind the discontinuous jump.

In this paper we did not discuss the details of the emission line spectra because obtained by now results are insufficient for comparison with observations. The change of the velocity of the gas during its passage through the shock wave must inevitably influence the line profiles. Calculations of the shock wave structure based on the solution of the transfer equation which takes into account effects of the gas flow velocity gradient were beyond the scope of the present work and will be presented in the forthcoming paper.

Acknowledgements. The work of YAF has been done in part under the auspices of the Aix-Marseille I University and CNRS. YAF acknowledges also the support from the Russian Foundation for Basic Research (grant 98–02–16734).

References

Abt, H. A., 1954, ApJS 1, 63
Alvarez, R., Jorissen, A., Plez, B., et al., 2000, A&A, in press
Bowen, G. H., 1988, ApJ 329, 299
Fadeyev, Y. A. & Gillet, D., 1998, A&A 333, 687 (Paper I)
Fadeyev, Y. A. & Gillet, D., 2000, A&A 354, 349 (Paper II)
Fadeyev, Y. A. & Muthsam, H., 1990, A&A 234, 188
Fadeyev, Y. A. & Tutukov, A. V., 1981, MNRAS 195, 811
Fox, M. W., Wood, P. R., Dopita, M. A., 1984, ApJ 286, 337
Gillet, D., Duquennoy, A., Bouchet, P., et al., 1989, A&A 215, 316
Gillet, D., Maurice, E., Bouchet, P., et al., 1985, A&A 148, 155
Klein, R. I., Stein, R. F., Kalkofen, W., 1976, ApJ 205, 499
Klein, R. I., Stein, R. F., Kalkofen, W., 1978, ApJ 220, 1024
Lèbre, A. & Gillet, D., 1992, A&A 255, 221
Marshak, R. E., 1958, Phys.Fluids 1, 24
Mihalas, D. & Weibel Mihalas, B., 1984, "Foundations of radiation hydrodynamics", New York: Oxford University Press, 1984
Pijpers, F. P., 1993, A&A 267, 471
Unno, W., 1965, PASJ 17, 205
Willson, L. A., 1976, ApJ 205, 172
Willson, L. A. & Hill, S. J., 1979, ApJ 228, 854
Wood, P. R., 1974, ApJ 190, 609
Wood, P. R., 1979, ApJ 227, 220